Available online at www.sciencedirect.com
SCIENCE DIRECT®
International Journal of Solids and Structures 42 (2005) 1327–1354
INTERNATIONAL JOURNAL OF SOLIDS and STRUCTURES
www.elsevier.com/locate/ijsolstr

A numerical model for reinforced concrete structures

T. Rabczuk *, J. Akkermann, J. Eibl

Institute of Concrete Structures and Building Materials, University of Karlsruhe, 76128, Germany

Received 19 July 2004; received in revised form 20 July 2004
Available online 25 September 2004

Abstract

This paper describes a two-dimensional approach to model fracture of reinforced concrete structures under (increasing) static loading conditions. The first part is dedicated to the concrete material. The concrete is described in compression by a non-local isotropic damage constitutive law. In tension, a fictitious crack/crack band model is proposed. The influence of biaxial stress states is incorporated in the constitutive relations. In the second part a bond model is described. It accounts for different failure mechanisms, a pullout failure and a splitting failure. This approach is applied to prestressed concrete beams with different failure mechanisms. The numerical results are compared to experimental data and show good agreement.

1. Introduction

Crack initiation and propagation plays a significant role in engineering problems for a long time. The fracture of reinforced concrete structures under monotonic increasing load conditions such as prestressed beams or frame corners are for us of interest. Cracking is crucial in the fracture process of reinforced concrete structure. Many theories about crack models in a finite element analysis can be found in the literature. The crack models can be classified into two groups. The first group tries to smear the crack (the crack is considered to be fictitious) and the second group treats the crack as *discrete*, meaning as a real discontinuity.

In early approaches the crack is modelled by a strain softening in the stress–strain curve, see e.g. Lemaitre (1971). Such continuum models are mesh-dependent if no arrangements are made since a finer discretization leads to a decreasing fracture energy. Other approaches are fictitious crack and smeared crack models, see e.g. Hillerborg et al. (1976) or Jirasek and Zimmermann (1998). In those models, a crack is

* Corresponding author. Address: Department of Mechanical Engineering, Northwestern University, 2145 Sheridan Road, Evanston, IL 60208-311, USA. Tel.: +1 847 491 3046; fax: +1 847 491 3915.
E-mail address: t-rabczuk@northwestern.edu (T. Rabczuk).

0020-7683/$ - see front matter © 2004 Elsevier Ltd. All rights reserved.
doi:10.1016/j.ijsolstr.2004.07.019

assumed to be within an element. Usually the strains are related to a '*fictitious*' crack width in the elements. In smeared crack models, it has to be distinguished if a single or several cracks should be modelled within a single-finite element. If larger structure such as shells are of interest, more than one crack can be initiated in an element. The advantage of smeared crack models is that the cracks are initiated randomly in contrast to discrete crack models but the crack is not considered as discontinuity. Other approaches are microplane model, see e.g. Bazant and Prat (1988), Bazant et al. (1996), Bazant et al. (2000) or Carol and Bazant (1997). A good overview can be found in Jirasek (1993).

Discrete crack models are an alternative to fictitious crack models. Here, a discontinuity is introduced. One of the possibilities for introducing discrete cracks is to separate elements along their boundaries, see e.g. Xu and Needleman (1996). This approach has the disadvantage that the crack propagation depends on the geometry of the elements and the topology of the mesh. Remeshing and refinement can overcome this drawback but they are computationally expensive. The Cornell group of Ingraffea follows the latter idea. Recently, discrete crack methods were developed where the crack can propagate arbitrary in an element without remeshing, see e.g. Samaniego et al. (2003), Belytschko and Black (1999), Belytschko et al. (2001) and Wells and Sluys (2001).

If the crack is treated as a discontinuity, meshfree methods are a good alternative to finite elements. Modelling cracks in meshfree methods were proposed e.g. by Belytschko et al. (1994, 1995). However, meshfree methods are computationally more expensive than finite elements.

A smeared/fictitious crack model was used. The commercial code ABAQUS was chosen because it offers the user the possibility to implement own elements and constitutive laws. The model is a combination and extension of different models, see Section 2. A combined rotating-fixed crack approach is proposed which has advantages over pure rotating or pure fixed crack models as will be shown in Section 2.1. In compression, a non-local scalar damage model is applied which is similar to a model proposed by Bazant and Ozbolt (1990) but easier to implement since only minor changes in the 'local' stress–strain curves have to be made. The approach is extended for strength decreases and increases under two-dimensional stress states.

For reinforced concrete structures, not only cracking of concrete plays a significant role but also the interaction between concrete and the reinforcement. A bond model developed originally by Den Ujil and Bigaj (1996) is modified which can produce all significant bond failure mechanisms. The bond model is implemented as user element into ABAQUS. Using the concrete constitutive model together with the bond model, the complicated behavior of different concrete structures was reproduced quite well.

The article is arranged as follows: In the next section, the constitutive law for concrete is explained. In Section 3 and 4, the approach for the reinforcement and the bond model is reviewed. Finally, our model is applied to prestressed concrete beams. The numerical results are compared to experimental data and show a good agreement.

2. The constitutive model for concrete

The constitutive model for concrete is a fictitious/smeared crack model in tension and a non-local scalar damage model in compression. Unloading is purely elastic, meaning no plastic deformations occur. This limits the application of the model since it is not well suited for modelling cyclic loading behavior. Since structures at monotonic increasing load conditions are of interest, this model is sufficient enough to capture all desired failure mechanisms as will be shown in some applications in Section 5.

2.1. Tensile loading

The tensile behavior of concrete is described with a fictitious/smeared crack model. In this approach, the stress is formulated in terms of relative displacements instead of strains. It is well known that a stress strain

relation leads to mesh-dependency since with finer discretization the fracture energy G_f is decreasing. Bazant and Oh (1983) eliminated the mesh dependency using a crack band model with constant fracture energy G_f. In this approach, the crack width w is related to the strain ϵ_c perpendicular to the crack via a characteristic element length l_{ch}:

$$w = l_{ch}\epsilon_c \tag{1}$$

with $l_{ch} = \sqrt{A_{el}}$ where A_{el} is the area of the element. Nevertheless, a complete mesh-independence can be achieved only if the crack is parallel to the element sides since for diagonal cracks the crack band goes over the neighboring elements. Ozbolt (1995) showed that mesh independency can be achieved with non-local approaches, but the process zone has to be modelled with several elements which requires a very fine discretization. A fictitious/smeared crack model is chosen since mainly the orientation of the cracks rather than their nucleation is of interest.

According to the fictitious crack model of Hillerborg et al. (1976), the fracture energy G_f can be expressed in terms of stress–displacement relation, see Fig. 2

$$G_f = \int_0^{w_1} \sigma_c \, dw \tag{2}$$

where σ_c is the stress in the crack band and w_1 is the crack width with $\sigma_c = 0$. Hillerborg et al. (1976) set the crack width to zero after exceeding the tensile strength as illustrated in Fig. 1. The domain $0 < w \leqslant w_1$ is called the process zone where many microcracks evolve. After exceeding w_1, a macrocrack occurs.

The stress-crack width relation before crack initiation can be described by linear elastic material behavior as shown in Fig. 2. A crack is initiated when the tensile stress σ_i exceeds the tensile strength f_{ct} (this is well known as Rankine criterion) where the subscript i indicates an arbitrary direction. In the following the stress strain relation for a uniaxial arbitrary directed load is given. The crack will be perpendicular to the principal tensile strain as described later.

The stress-crack width relation in the softening region is approximated via a bilinear relationship according to Roelfstra and Wittmann (1986). The parameter α_t is set to 0.14 while $\beta_t = 0.25$ for concrete with a compressive strength f_c less than 30 MPa and $\beta_t = 0.25$–0.0015 (f_c [MPa] $- 30$) if $f_c > 30$ MPa. The crack width w_c is computed as

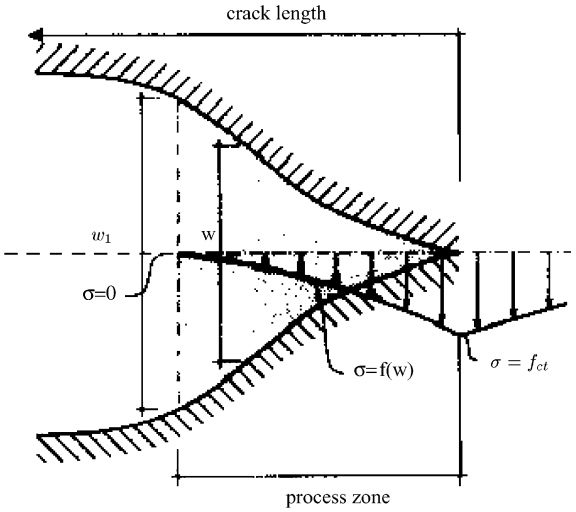

Fig. 1. Fictitious crack model according to Hillerborg et al. (1976).

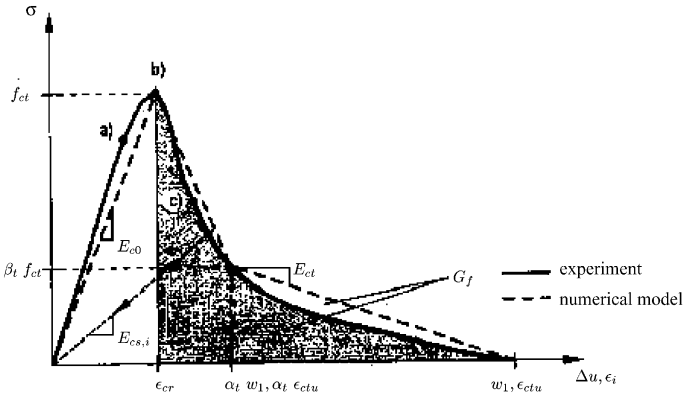

Fig. 2. Stress–deformation relation for the uniaxial tensile test and the stress–strain relation for the numerical model.

$$w_1 = \frac{2G_f}{f_{ct}(\alpha_t + \beta_t)} \tag{3}$$

For the crack band model according to Bazant and Oh (1983), a fictive crack strain is given by

$$\epsilon_{ctu} = \frac{w_1}{l_{ch}} \tag{4}$$

The stress–strain relation can now be divided into four regions. The stress in the corresponding direction is computed as

$$\sigma_i = E_{cs,i}\epsilon_i \tag{5}$$

where $E_{cs,i}$ is the corresponding secant stiffness. The secant and the tangent stiffness $E_{ct,i}$ for the four domains are (see Akkermann, 2000 and Fig. 2):

Domain 1: $0 \leqslant \epsilon_i \leqslant \epsilon_{cr} = f_{ct}/E_{c0}$

$$\begin{aligned} E_{cs,i} &= E_{c0} \\ E_{ct,i} &= E_{c0} \end{aligned} \tag{6}$$

where E_{c0} is the initial Young's modulus and ϵ_{cr} is the strain which corresponds to f_{ct}.

Domain 2: $\epsilon_{cr} \leqslant \epsilon_i \leqslant \epsilon_{cr} + \alpha_t \epsilon_{ctu}$

$$\begin{aligned} E_{cs,i} &= E_{soft1} + \frac{f_{ct}(1 - E_{soft1}/E_{c0})}{\epsilon_i} \\ E_{ct,i} &= E_{soft1} \\ E_{soft1} &= (\beta_t - 1)\frac{f_{ct}}{\alpha_t \epsilon_{ctu}} \end{aligned} \tag{7}$$

where ϵ_{ctu} corresponds to w_1 when a macrocrack has evolved, see also Fig. 2 and 1.

Domain 3: $\epsilon_{cr} + \alpha_t \epsilon_{ctu} \leqslant \epsilon_i \leqslant \epsilon_{cr} + \epsilon_{ctu}$

$$\begin{aligned} E_{cs,i} &= E_{soft2} + \frac{f_{ct}(\beta_t f_{ct} - \alpha_t \epsilon_{ctu} + \epsilon_{cr})}{\epsilon_i} \\ E_{ct,i} &= E_{soft2} \\ E_{soft2} &= (0.001 - \beta_t)\frac{f_{ct}}{(1 - \alpha_t)\epsilon_{ctu}} \end{aligned} \tag{8}$$

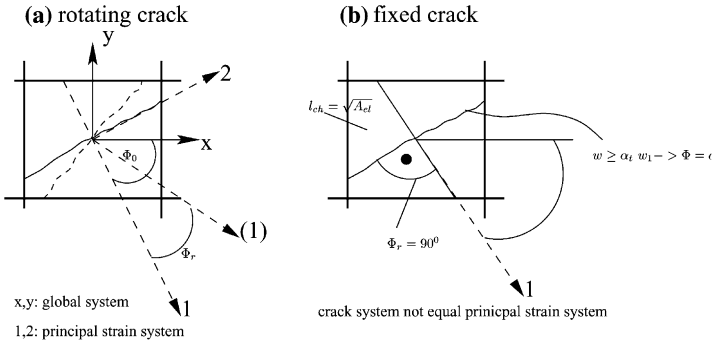

Fig. 3. Fixed cracks and rotating cracks.

Domain 4: $\epsilon_{cr} + \epsilon_{ctu} \leqslant \epsilon_i$

$$E_{cs,i} = \frac{0.001 f_{ct}}{\epsilon_i}$$
$$E_{ct,i} = 0 \tag{9}$$

For numerical reasons, the tensile stress in region 4 is not set completely to zero.

There are different smeared crack approaches which are discussed in detail by Rots (1988). They can be classified into fixed single cracks, fixed orthogonal cracks, fixed multiaxial cracks and rotating cracks, see also Fig. 3. In most fixed crack models, the crack system does not correspond to the principal strain system if the direction of the loading changes. Often too stiff answers were observed. In rotating crack models the crack rotates with the principal strain. In these cases, very soft system answers were observed.

A combined fixed-rotating crack model is proposed. Until a certain crack width $w_{\text{rot-fix}} = \alpha_t w_1$ (see Fig. 2), the crack rotates with the principal tensile strain system. This guarantees that the material can deform in arbitrary directions. At the crack width $w_{\text{rot-fix}}$ where a full discontinuity is initiated, the crack is fixed. This prevents unrealistic crack directions. Once the crack is fixed, another crack can evolve only perpendicular to the existing crack.

For rotating cracks, there are no shear stresses and the normal stresses can be computed directly from the principal strains:

$$\begin{bmatrix} \sigma_1 \\ \sigma_2 \end{bmatrix} = \begin{bmatrix} E_{cs,1} & 0 \\ 0 & E_{cs,2} \end{bmatrix} \begin{bmatrix} \epsilon_1 \\ \epsilon_2 \end{bmatrix} \tag{10}$$

Nevertheless, for the computation of the element stiffness, a tangential shear stiffness is necessary. Rots (1988) and Willam et al. (1987) have shown that the direction of principal stresses and principal strains have to be the same if the crack system is parallel to the principal strain system. With the direction angles

$$\tan 2\phi_\sigma = \frac{\Delta\tau_{12}}{(\sigma_1 + \Delta\sigma_{11}) - (\sigma_2 + \Delta\sigma_{22})} \tag{11}$$

$$\tan 2\phi_\epsilon = \frac{\Delta\gamma_{12}}{2[(\epsilon_1 + \Delta\epsilon_{11}) - (\epsilon_2 + \Delta\epsilon_{22})]} \tag{12}$$

and with $\phi_\sigma = \phi_\epsilon$, the tangent shear stiffness G_{ct} is

$$G_{ct} = \frac{\Delta\tau_{12}}{\Delta\gamma_{12}} = \frac{(\sigma_1 + \Delta\sigma_{11}) - (\sigma_2 + \Delta\sigma_{22})}{2[(\epsilon_1 + \Delta\epsilon_{11}) - (\epsilon_2 + \Delta\epsilon_{22})]} \tag{13}$$

where $\Delta\gamma_{12}$ are the engineering strains.

For fixed cracks, the crack system is not any more parallel to the principal strain system and shear stresses can evolve along the crack edges. Walraven (1980) has shown a dependence between the shear stiffness and the crack width which is taken into account by shear reduction factors η, so that the secant shear stiffness can be written as

$$\begin{aligned} G_{cs} &= \eta_{\tau,1}\eta_{\tau,2}\frac{E_{cs,c}}{2(1+\nu_0)} \\ \eta_{\tau,i} &= \left(1-\frac{w_i}{w_1}\right)^a \quad \forall 0 \leqslant w_i \leqslant w_1 \\ \eta_{\tau,i} &= 0 \quad \forall w_1 \leqslant w_i \end{aligned} \tag{14}$$

where $E_{cs,c}$ is the stiffness of the uncracked concrete, ν_0 is the Poisson ratio and a is a material parameter. Rots (1992) has shown that shear reduction factors avoid stress locking. Jirasek and Zimmermann (1998) have shown that stress locking for rotating crack models can also be avoided by switching to scalar damage models.

2.2. Compressive loading

Micromechanical investigation for uniaxial compression tests have shown that the softening behavior of concrete depends on the dimensions of the specimen, see e.g. van Mier (1984) and Vonk (1993). Fig. 4 shows the stress strain and stress deformation curve, respectively, for specimens of different height. The smaller the height of the specimen the more ductile is the material behavior. This effect can be explained as follows: Under uniaxial compression, cracks will evolve perpendicular to the direction of the maximum principal strain. For a uniaxial load, this will be perpendicular to the load direction. Little columns evolve as shown in Fig. 5. The softening behavior is mainly characterized by the stability of these 'columns'. The shorter the critical buckling length the more ductile will be the material response.

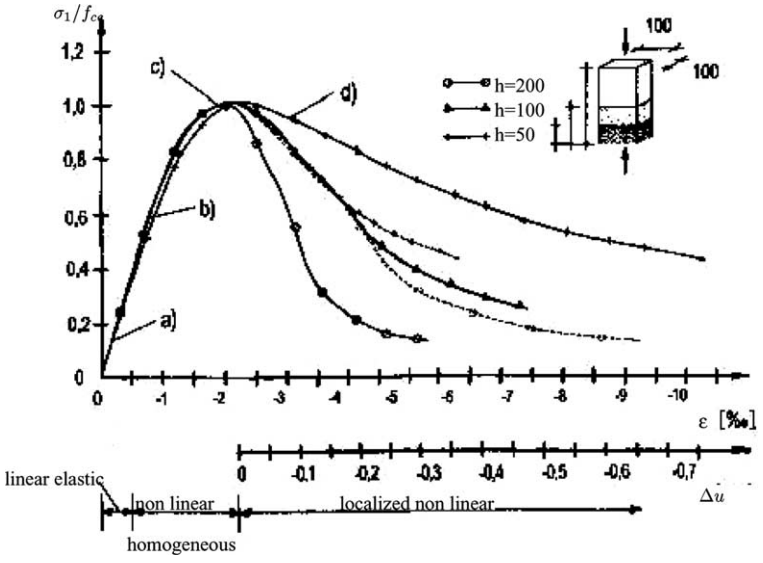

Fig. 4. Uniaxial compressive test by van Mier (1984).

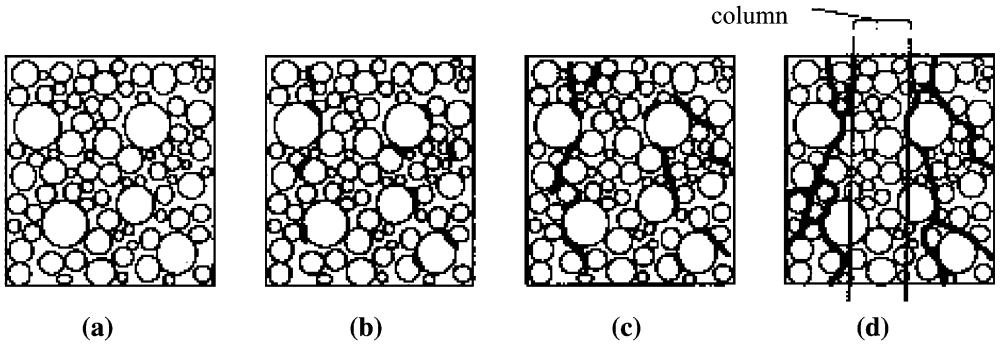

Fig. 5. Failure mechanisms of concrete in compression.

For biaxial loading conditions, the failure surface of concrete can be characterized as in Kupfer (1973), see also Fig. 6:

$$f_{c,\mathrm{eff}} = \eta_c f_{c0} \tag{15}$$

with

$$\eta_c = \frac{1 + 3.65\sigma_2/\sigma_1}{(1 + \sigma_2/\sigma_1)^2}, \quad \epsilon_{c,\mathrm{eff}} = (3\eta_c - 2)\epsilon_{c1} \tag{16}$$

$$\eta_c = \frac{1 + 3.28\sigma_2/\sigma_1}{(1 + \sigma_2/\sigma_1)^2} > 0.65, \quad \epsilon_{c,\mathrm{eff}} = \eta_c \epsilon_{c1} \tag{17}$$

where f_{c0} is the uniaxial compressive strength, ϵ_{c1} is the corresponding strain and σ_i, $i = 1,2$ are the principal stresses. Eibl and Neuroth (1988) and Kolleger and Mehlhorn (1990) studied the influence of shells under compressive-tensile loads and suggest to replace the principal stresses by principal strains in Eq. (17).

The scalar damage model to describe concrete in compression is given by

$$\sigma = (1 - D_c) E_{c0}\, \epsilon \tag{18}$$

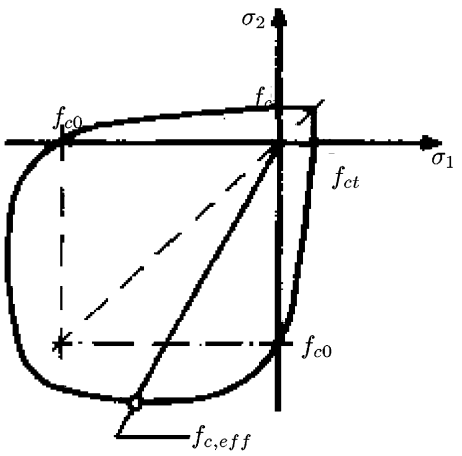

Fig. 6. Biaxial failure surface of concrete.

where D_c is a damage variable and E_{c0} is the Young's modulus. The damage variable is computed by

$$D_c = 1 - \frac{E_{cs,c}}{E_{c0}} \tag{19}$$

where $E_{cs,c} = (1 - D) E_{c0}$ is the secant stiffness. According to the effective stress strain curve in Fig. 7, the secant $E_{cs,c}$ and the tangent stiffness $E_{ct,c}$ can be calculated to:

Domain 1: see MC90, 1993: $0 > \tilde{\epsilon}_c \geqslant \epsilon_{c,eff}$

$$\begin{aligned} E_{cs,c} &= \frac{E_{c0} - f_{c,eff}\frac{\tilde{\epsilon}_c}{\epsilon^2_{c,eff}}}{1 + \frac{E_{c0}\tilde{\epsilon}_c}{f_{c,eff}} - 2\frac{\tilde{\epsilon}_c}{\epsilon_{c,eff}}} \\ E_{ct,c} &= f^2_{c,eff}\frac{E_{c0}\epsilon^3_{c,eff} - 2\tilde{\epsilon}_c\epsilon_{c,eff}f_{c,eff} - E_{c0}\tilde{\epsilon}^2_c\epsilon_{c,eff} + 2\tilde{\epsilon}^2_c f_{c,eff}}{\left(f_{c,eff}\epsilon_{c,eff} + E_{c0}\tilde{\epsilon}_c\epsilon_{c,eff} - 2\tilde{\epsilon}_c f_{c,eff}\right)^2} \end{aligned} \tag{20}$$

where $\tilde{\epsilon}_c$ is the equivalent uniaxial compressive strain.

Domain 2: $\epsilon_{c,eff} > \tilde{\epsilon}_c \geqslant \epsilon_{cc} = \epsilon_{c,eff} + \Delta\epsilon_{con}$

$$\begin{aligned} E_{cs,c} &= \frac{f_{c,eff}}{\tilde{\epsilon}_c} \\ E_{ct,c} &= 0 \end{aligned} \tag{21}$$

Domain 3: $\epsilon_{cc} > \tilde{\epsilon}_c \geqslant \epsilon_{ccu,eff}$

$$\begin{aligned} E_{cs,c} &= \frac{f_{c,eff}}{\tilde{\epsilon}_c} + E_{c,soft}\left(1 - \frac{\epsilon_{cc}}{\tilde{\epsilon}_c}\right) \\ E_{ct,c} &= E_{c,soft} \end{aligned} \tag{22}$$

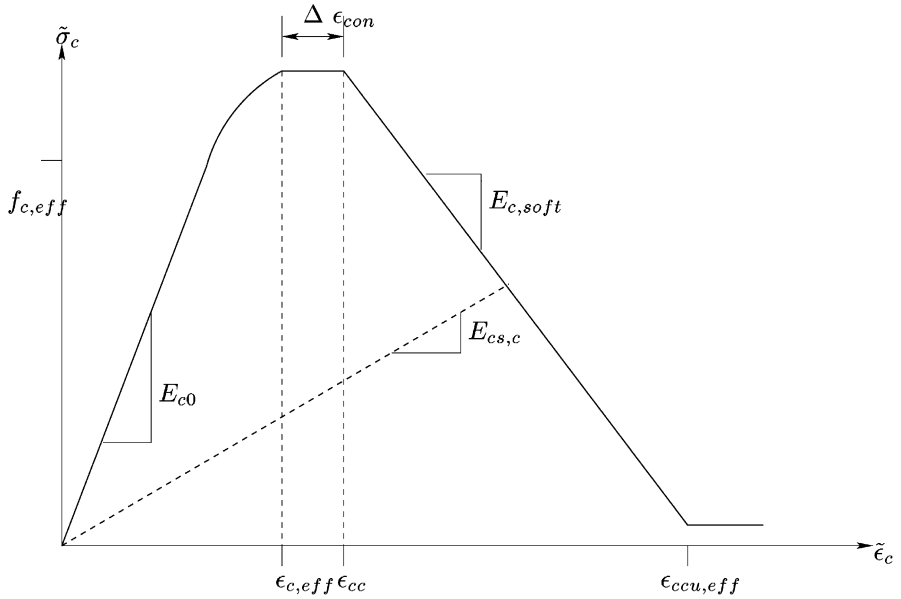

Fig. 7. Uniaxial stress–strain curve of concrete under compressive loading.

Domain 4: $\epsilon_{\mathrm{ccu}}, eff > \tilde{\epsilon}_{\mathrm{c}}$

$$E_{\mathrm{cs,c}} = \frac{0.0001\ f_{\mathrm{c,eff}}}{\tilde{\epsilon}_{\mathrm{c}}}$$
$$E_{\mathrm{ct,c}} = 0 \tag{23}$$

The shape of the stress–strain curve in the softening region was investigated by several authors, see e.g. Bazant (1998), van Mier et al. (1997) or Jansen and Shah (1997) and is still topic of ongoing research. A fracture mechanic approach of Markeset and Hillerborg (1995) is chosen, which was applied successfully by Belytschko et al. (2001) and Meyer and Koenig (1998). In this approach, the softening modulus $E_{\mathrm{c,soft}}$ is computed by

$$E_{\mathrm{c,soft}} = \frac{0.0001 f_{\mathrm{c0}} - f_{\mathrm{c,eff}}}{\epsilon_{\mathrm{ccu,eff}} - \epsilon_{\mathrm{cc}}} \tag{24}$$

where f_{c0} is the uniaxial compressive strength. A detailed description of the model can be found in Markeset and Hillerborg (1995) or Akkermann (2000).

2.3. Stiffness matrices

As mentioned in the introduction, the constitutive model is implemented in the finite element Code ABAQUS as user subroutine. Plane stress conditions are assumed with engineering strains $\gamma_{12} = \epsilon_{12} + \epsilon_{21}$.

If the material is not cracked, the secant stiffness matrix can be expressed in terms of the secant stiffness $E_{\mathrm{cs,c}}$

$$\mathbf{C}_s = \frac{E_{\mathrm{cs,c}}}{1-\nu_0^2}\begin{bmatrix} 1 & \nu_0 & 0 \\ \nu_0 & 1 & 0 \\ 0 & 0 & 0.5(1-\nu_0) \end{bmatrix} \tag{25}$$

If the concrete is cracked, the stiffness matrix becomes anisotropic, i.e. $C_{11} \neq C_{22}$. The Poisson ratio parallel to the crack is

$$\begin{aligned} \nu_i &= \nu_0, \quad w = 0 \\ \nu_i &= 0, \quad w = w_1 \end{aligned} \tag{26}$$

where i is defined by the direction normal to the crack plane. The Poisson ratio perpendicular to the crack is proportional to the secant stiffness ($\nu_i\ E_{\mathrm{cs},i}$) with the conditions:

$$\begin{aligned} &E_{\mathrm{cs},i} = E_{\mathrm{cs,c}} \Rightarrow \nu_i = \nu_0 \\ &E_{\mathrm{cs},i} = 0 \Rightarrow \nu_i = 0 \end{aligned} \tag{27}$$

Because of symmetry conditions, $\nu_1 E_{\mathrm{cs},2} = \nu_2 E_{\mathrm{cs},1}$. Hence, the anisotropic Poisson ratio can be formulated as

$$\nu_i = \nu_0 \frac{E_{\mathrm{cs},i}}{E_{\mathrm{cs,c}}} \tag{28}$$

and the secant stiffness matrix according to the crack coordinate system is given by

$$\mathbf{C}_s = \frac{1}{1-\nu_1\nu_2}\begin{bmatrix} E_{\mathrm{cs},1} & \nu_2 E_{\mathrm{cs},1} & 0 \\ \nu_1 E_{\mathrm{cs},2} & E_{\mathrm{cs},2} & 0 \\ 0 & 0 & 0.5(1-\nu_1\nu_2)G_{\mathrm{cs}} \end{bmatrix} \tag{29}$$

For the secant stiffness $E_{\mathrm{cs},i}$, the maximum between tensile and compressive damage is relevant so that $E_{\mathrm{cs},i} \leqslant E_{\mathrm{cs,c}}$. Until the crack is considered as fixed crack, the principal strain system is regarded as reference coordinate system. The stress and strain vector, respectively, as well as the stiffness matrices have to be transformed into the reference system:

$$\boldsymbol{\sigma}^* = \begin{bmatrix} cc & ss & 2cs \\ ss & cc & -2cs \\ -cs & cs & cc-ss \end{bmatrix} \boldsymbol{\sigma} = \mathbf{T}_\sigma \boldsymbol{\sigma} \tag{30}$$

$$\boldsymbol{\epsilon}^* = \begin{bmatrix} cc & ss & cs \\ ss & cc & cs \\ -2cs & 2cs & cc-ss \end{bmatrix} \boldsymbol{\epsilon} = \mathbf{T}_\epsilon \boldsymbol{\epsilon} \tag{31}$$

$$\mathbf{C}^* = \mathbf{T}_\epsilon \, \mathbf{C} \, \mathbf{T}_\epsilon \tag{32}$$

with $c = \cos(\phi_\epsilon)$, $s = \sin(\phi_\epsilon)$.

To compute the secant and tangent stiffness, respectively, the concept of equivalent uniaxial strains (see Darwin and Pecknold, 1977) is used. With

$$\tilde{\epsilon}_1 = \frac{\epsilon_{11} + \nu_2 \epsilon_{22}}{1 - \nu_1 \, \nu_2} \tag{33}$$

$$\tilde{\epsilon}_2 = \frac{\nu_1 \epsilon_{11} + \epsilon_{22}}{1 - \nu_1 \nu_2} \tag{34}$$

the stress strain relation can be written as

$$\begin{bmatrix} \sigma_{11} \\ \sigma_{22} \\ \tau_{12} \end{bmatrix} = \begin{bmatrix} E_{\mathrm{cs},1} & 0 & 0 \\ 0 & E_{\mathrm{cs},2} & 0 \\ 0 & 0 & G_{\mathrm{cs}} \end{bmatrix} \begin{bmatrix} \tilde{\epsilon}_1 \\ \tilde{\epsilon}_2 \\ \gamma_{12} \end{bmatrix} \tag{35}$$

The equivalent uniaxial strains can be expressed by $\tilde{\epsilon}_i = \sigma_{ii}/E_{\mathrm{cs},i}$. If $\tilde{\epsilon}_i \geqslant 0$ (tensile loading), the secant and tangent stiffness is computed by Eq. (6)–(9). A fictitious crack width $\tilde{w}_i$ is defined

$$\begin{aligned} &\tilde{w}_i = l_{\mathrm{ch}} \left(\tilde{\epsilon}_i - \frac{E_{\mathrm{cs},i} \tilde{\epsilon}_i}{E_{\mathrm{cs,c}}} \right), \quad \tilde{\epsilon}_i \geqslant 0 \\ &\tilde{w}_i = 0, \quad \tilde{\epsilon}_i < 0 \end{aligned} \tag{36}$$

The equivalent compressive strains are $\tilde{\epsilon}_{\mathrm{c}} = \min[\tilde{\epsilon}_1, \tilde{\epsilon}_2] \leqslant 0$. The third line in Eq. (35) is the shear stress–shear deformation relation. For the non-cracked concrete, Eq. (25) applies. For rotating cracks, no shear stresses occur in the crack system as explained in Section 2.1. For fixed cracks, Eq. (13) applies. The stresses in the reference system have to be transformed back to the global coordinate system by use of the transformation matrix $\mathbf{T}_\sigma$, see Eq. (30), where $-\phi_\epsilon$ has to be used.

2.4. Loading, unloading, reloading

Even at monotonic increasing loading conditions, unloading can occur locally. At unloading and reloading conditions, the damage of the material has to be constant, i.e. $\dot{D} = 0$. The increase of tensile and compressive damage $\dot{D}_{\mathrm{c}}$ and $\dot{D}_{\mathrm{t},i}$, respectively, can be defined by

$$\dot{D}_{\mathrm{c}} = f(< -\tilde{\epsilon}_{\mathrm{c}} >) > 0, \quad \text{if } \dot{\tilde{\epsilon}}_{\mathrm{c}} < 0 \text{ and } \tilde{\epsilon}_{\mathrm{c}} \leqslant \tilde{\epsilon}_{\mathrm{c,min}} \tag{37}$$

$$\dot{D}_{t,i} = f(< \tilde{\epsilon}_i >) > 0, \quad \text{if } \dot{\tilde{\epsilon}}_i > 0 \text{ and } \tilde{\epsilon}_i \geqslant \tilde{\epsilon}_{i,\max} \tag{38}$$

with the McAuley brackets $\langle x \rangle = 0.5(x + |x|)$ and where $\tilde{\epsilon}_{c,\min}$ and $\tilde{\epsilon}_{i,\max}$ are the minimum of the equivalent compressive strain and the maximum of the equivalent tensile strain, respectively, within the load history. If the damage is constant, the secant stiffness stays the same and is equivalent to the tangent stiffness.

Let us consider a constant tensile damage and an increasing compressive damage, e.g. if a crack closes. Since the damage is irreversible and the compressive damage is isotropic, the compressive damage influences also the tensile damage (see Eq. (27)). This takes into account that a complete damaged concrete in compression cannot withstand tensile loading anymore. Stresses parallel to the crack can still be transmitted.

2.5. Non-local compressive damage

Bazant (1991) and Bazant (1998) showed that local approaches in the softening region of the stress strain relation lead to poor results. An alternative to local approaches are non-local approaches, see e.g. Bazant and Pihaudier-Gabot (1988) or De Vree et al. (1995). An approach developed by Bazant and Ozbolt (1990) is adopted. In this approach, the strain field is smeared with a weighting function. Since our model for compressive damage is isotropic- in contrast to their anisotropic model- only the compressive strain has to be smeared. Since the compressive damage variable D_c is a scalar, smearing the compressive strain field is equivalent to smearing D_c:

$$\bar{D}_c(\mathbf{x}) = \frac{1}{V_r(\mathbf{x})} \int_V \alpha_{nl}(\mathbf{s} - \mathbf{x})\ D_c(\mathbf{s})\, dV_{(s)} \tag{39}$$

where α_{nl} is the geometric weighting function which relates the damage at point $\mathbf{x}$ to the neighboring points $\mathbf{s}$:

$$\begin{aligned} &\alpha_{nl}(\mathbf{s} - \mathbf{x}) = \left(1 - \left[\frac{|\mathbf{s} - \mathbf{x}|}{R}\right]^2\right)^2, \ |\mathbf{s} - \mathbf{x}| \leqslant R \\ &\alpha_{nl}(\mathbf{s} - \mathbf{x}) = 0, \ |\mathbf{s} - \mathbf{x}| > R \end{aligned} \tag{40}$$

with

$$\int_0^{2\pi} \int_0^R \alpha_{nl}\, dr\, d\phi = 1\pi\ \frac{L_d^2}{4} \tag{41}$$

and

$$\begin{aligned} r = |\mathbf{s} - \mathbf{x}| \quad &= \quad \sqrt{(s_1 - x_1)^2 + (s_2 - x_2)^2} \\ \tan\phi = \tfrac{s_2 - x_2}{s_1 - x_1} \end{aligned} \tag{42}$$

we obtain

$$R = 0.75^{1/3} \quad L_d = 0.90856\ L_d \tag{43}$$

The parameter L_d is calibrated so that the volume under the curve α_{nl} corresponds to the volume of a cylinder of diameter L_d, see Fig. 8. The representative volume $V_r(\mathbf{x})$ in Eq. (39) is

$$V_r(\mathbf{x}) = \int_V \alpha_{nl}(\mathbf{s} - \mathbf{x})\, dV_{(s)} \tag{44}$$

Note, that the influence of $\mathbf{s}$ according to $\mathbf{x}$ is symmetric. Ozbolt (1995) showed that smearing only the strain field leads to poor results. He showed that the influence of the neighboring point $\mathbf{s}$ according to $\mathbf{x}$

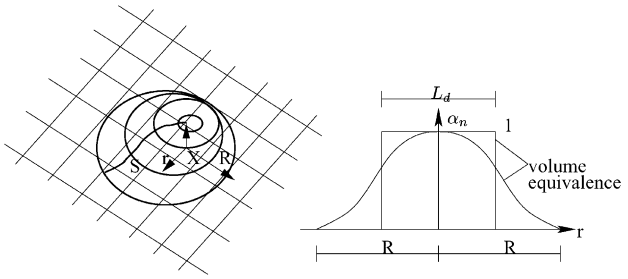

Fig. 8. Weighting function according to Eq. (40).

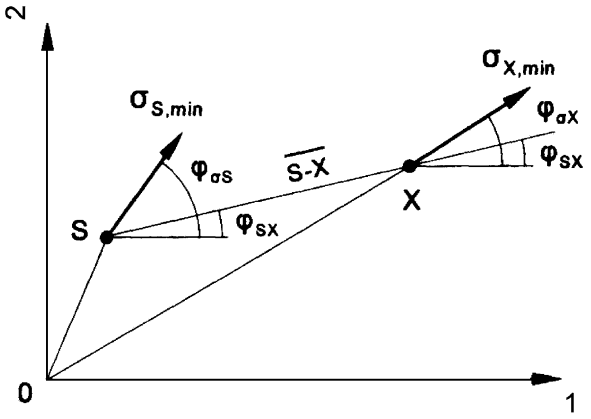

Fig. 9. Geometric conditions for the determination of the influence of the stress direction.

increases if the direction of the compressive stress coincides in both points which leads to a stress direction weighting function as shown in Fig. 9. This approach is adopted. Therefore, the angle φ_{SX} according to Fig. 9 is computed:

$$\varphi_{SX} = \arctan\frac{s_2 - x_2}{s_1 - x_1} (= 0.5\pi \quad \text{if } s_1 - x_1 = 0) \tag{45}$$

The direction is bounded, $-0.5\pi \leqslant \varphi_{SX} \leqslant 0.5\pi$, so that for $|\varphi_{SX} \geqslant 0.5\pi|$

$$\varphi_{SX} = \varphi_{SX} - \text{sign}(\varphi_{SX})\ \pi \tag{46}$$

A Weibull distribution is chosen as weighting function (see Fig. 10) with

$$\begin{aligned} \varphi_{\sigma S} &= \mathrm{e}^{\left(-\frac{|\varphi_{SX}-\varphi_{\sigma S}|}{0.5\xi\ \pi}\right)^{\kappa}} \\ \varphi_{\sigma X} &= \mathrm{e}^{\left(-\frac{|\varphi_{SX}-\varphi_{\sigma X}|}{0.5\xi\ \pi}\right)^{\kappa}} \end{aligned} \tag{47}$$

where ξ and κ are material parameters. The non-local compressive damage reads now

$$\bar{D}_{\mathrm{c}}(\mathbf{x}) = \frac{1}{V_r(\mathbf{x})} \int_V \alpha_{\mathrm{nl}}(\mathbf{s}-\mathbf{x})\alpha_{\sigma S}(\mathbf{s},\mathbf{x})\alpha_{\sigma X}(\mathbf{s},\mathbf{x}) D_{\mathrm{c}}(\mathbf{s})\,\mathrm{d}V_{(s)} \tag{48}$$

and the representative volume

$$V_r(\mathbf{x}) = \int_V \alpha_{\mathrm{nl}}(\mathbf{s}-\mathbf{x})\alpha_{\sigma S}(\mathbf{s},\mathbf{x})\alpha_{\sigma X}(\mathbf{s},\mathbf{x})\,\mathrm{d}V_{(s)} \tag{49}$$

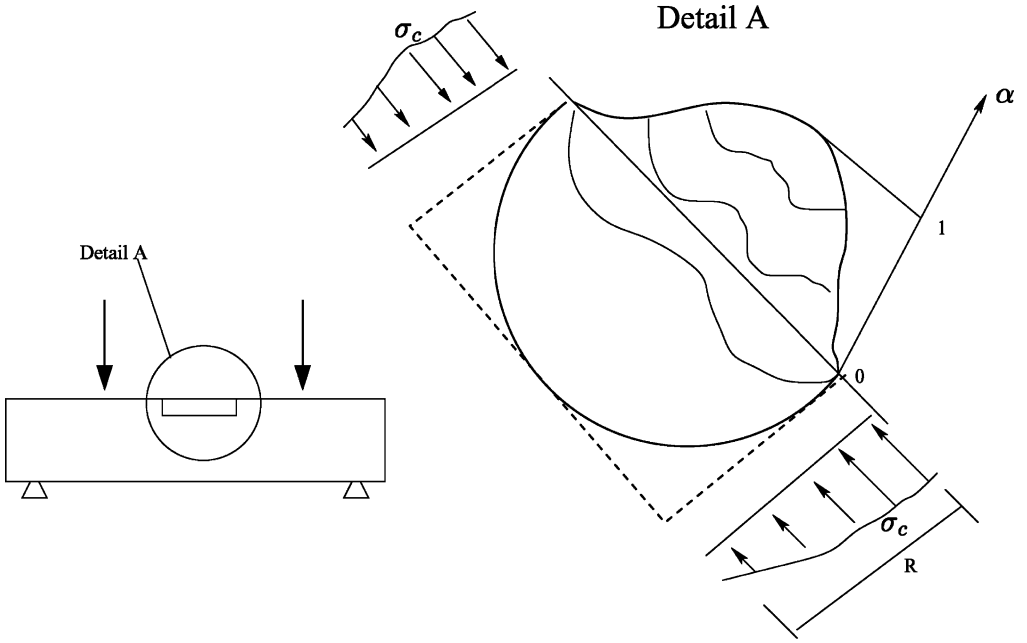

Fig. 10. Weighting function according to Eq. (48) in the compressive zone of a four point bending beam.

Fig. 10 shows the weighting function for a point close to the boundary for the beam shown in Fig. 10. The integrals (48) and (49) are evaluated numerically:

$$\bar{D}_c = \frac{\sum_{i=1}^{nel}\sum_{i=1}^{nint}\alpha_{nl}(\mathbf{s}_{ij}-\mathbf{x})\alpha_{\sigma S}(\mathbf{s}_{ij},\mathbf{x})\alpha_{\sigma X}(\mathbf{s}_{ij},\mathbf{x})\ D_c(\mathbf{s}_{ij})}{\sum_{i=1}^{nel}\sum_{i=1}^{nint}\alpha_{nl}(\mathbf{s}_{ij}-\mathbf{x})\alpha_{\sigma S}(\mathbf{s}_{ij},\mathbf{x})\ \alpha_{\sigma X}(\mathbf{s}_{ij},\mathbf{x})} \tag{50}$$

where *nel* and *nint* are the number of elements and integration points, respectively.

The stress–strain relation in compression is easily obtained by substituting the local damage variable D_c with the non-local damage variable $\bar{D}_c$ in Eq. (18). The shape of the stress–strain curve is the same as explained in Section 2.2 but using $\bar{D}_c$ instead of D_c now.

2.6. Numerical implementation of the concrete model

As mentioned before, the FE code ABAQUS is used for our numerical analysis which solves the following system of equations:

$$\mathbf{K}^{t+\Delta t}\ \Delta\mathbf{u}^{t+\Delta t} = \mathbf{R}^{t+\Delta t} - \mathbf{F}^{t} \tag{51}$$

where $\mathbf{K}^{t+\Delta t}$ is the incremental stiffness matrix at time $t+\Delta t$, $\Delta\mathbf{u}^{t+\Delta t}$ is the incremental displacement vector at time $t+\Delta t$, $\mathbf{R}^{t+\Delta t}$ are the external forces and $\mathbf{F}^{t}$ is the vector with the internal forces. Since (using nonlinear material behavior) $\mathbf{K}^{t+\Delta t}$ depends on the current displacement and stress state, an iteration is necessary to determine $\Delta\mathbf{u}^{t+\Delta t}$. A very common iteration scheme is the Newton Raphson iteration which is given by

$$\mathbf{K}_{n-1}^{t+\Delta t}\ \Delta\mathbf{u}_{n}^{t+\Delta t} = \mathbf{R}^{t+\Delta t} - \mathbf{F}_{n-1}^{t} \tag{52}$$

The displacements in the next iteration can be computed by

$$\mathbf{u}_n^{t+\Delta t} = \mathbf{u}_{n-1}^{t+\Delta t} + \Delta\mathbf{u}_n^{t+\Delta t} \tag{53}$$

with the initial values

$$\begin{aligned} \mathbf{u}_0^{t+\Delta t} &= \mathbf{u}^t \\ \mathbf{K}_0^{t+\Delta t} &= \mathbf{K}^t \\ \mathbf{F}_0^{t+\Delta t} &= \mathbf{F}^t \end{aligned} \tag{54}$$

A *total* stress–strain relation is used. The advantage of a total stress–strain formulation over an incremental one is that an accumulation of integration errors can be reduced. The actual stress state is determined by the actual strain and damage state. Since the actual damage depends also on the stress, an iteration on the material level (to determine the internal forces $\mathbf{F}_n^{t+\Delta t}$) is necessary since the damage depends on the stress state, too:

$$\boldsymbol{\sigma}^{t+\Delta t} = f(D^{t+\Delta t}, \boldsymbol{\epsilon}^{t+\Delta t}) = f(\boldsymbol{\sigma}^{t+\Delta t}, \boldsymbol{\epsilon}^{t+\Delta t}) \tag{55}$$

With the iteration scheme in Table 1, the stresses can easily be determined. The subscript n is the iteration index. In the first iteration step ($n = 1$), the stress tensor $\boldsymbol{\sigma}_n^{t+\Delta t}$ at time $t + \Delta t$ is computed using the secant stiffness matrix $\mathbf{C}_s$ at time t. After the stresses at iteration step n are computed, the secant stiffness $E_{n,\mathrm{cs},i}^{t+\Delta t}$ at iteration step n can be calculated. Therefore, the equivalent strains $\tilde{\epsilon}_{n,s}^{t+\Delta t}$ have to be computed before. With the new secant stiffness $E_{n,\mathrm{cs},i}^{t+\Delta t}$, the new secant stiffness matrix is assembled which will be compared to the secant stiffness matrix of the last iteration step $(n-1)$. If $\|\mathbf{C}_{n,s}^{t+\Delta t} - \mathbf{C}_{n-1,s}^{t+\Delta t}\| \leqslant TOL$, where TOL is a given threshold, the iteration is completed.

For materials with strain softening, the tangential stiffness matrix obtains negative values which leads to negative eigenvalues of the stiffness matrix $\mathbf{K}^{t+\Delta t}$ in Eq. (51). The solution is not unique any more. A common solution procedure for such kind of problems is the arc length control procedure, see e.g. Ramm (1981) or Schweitzerhof (1989) where an iteration for the external load is used, so that global instabilities can be computed. However, the crack initiation and propagation in concrete is a local instability which does not necessarily lead to the failure of the entire structure. Rots (1988) proposed an arc length control approach for the computation of a single crack but in our applications multiple cracks will occur. The results with the arc length control approach in ABAQUS did not give acceptable solutions.

Sluys (1992) and Etse and Willam (1999) showed that the uniqueness of the solution can be obtained by rate dependent or viscoelastic material models. Therefore, a viscous term is added to the constitutive model:

$$\boldsymbol{\sigma}^t = \mathbf{C}_s^t \boldsymbol{\epsilon}^t + \mathbf{V}\dot{\boldsymbol{\epsilon}}^t \tag{56}$$

Table 1
Iteration scheme

$\boldsymbol{\sigma}_n^{t+\Delta t} = \mathbf{C}_{n-1,s}^{t+\Delta t} \cdot \boldsymbol{\epsilon}^{t+\Delta t}$
$\tilde{\boldsymbol{\epsilon}}_{n,i}^{t+\Delta t} = \frac{\sigma_{n,i}^{t+\Delta t}}{E_{n-1,cs,i}^{t+\Delta t}}$
$E_{n,\mathrm{cs},i}^{t+\Delta t} = f(\tilde{\epsilon}_{n,i}^{t+\Delta t}, \boldsymbol{\sigma}_n^{t+\Delta t}) \rightarrow \mathbf{C}_{n,s}^{t+\Delta t}$
start: $\mathbf{C}_{0,s}^{t+\Delta t} = \mathbf{C}_s^t$
convergence if $\|\mathbf{C}_{n,s}^{t+\Delta t} - \mathbf{C}_{n-1,s}^{t+\Delta t}\| \leqslant TOL$

The viscosity matrix is given by

$$\mathbf{V} = \frac{V_c}{1-\nu^2}\begin{bmatrix} 1 & \nu_0 & 0 \\ \nu_0 & 1 & 0 \\ 0 & 0 & 0.5(1-\nu_0) \end{bmatrix} \tag{57}$$

V_c is not a material parameter and should not be confused with strain rate effects. A value of $V_c = 10.0$ is used in all our computations. Since for our kind of problems the orientation of the cracks rather than the crack nucleation is important, the error introduced by the viscosity seemed to be acceptable.

3. The reinforcement

The reinforcement is discretized with linear beam elements. An elasto-plastic constitutive model with isotropic hardening is used. The parameters of this model can be found in Section 5.1.

4. The bond model

4.1. Basics of the bond model

According to Cox and Herrmann (1998a,b), bond models can be developed at three different scales. The smallest scale is the *rib-scale*, where the geometry of the surface structure of the bar is modelled explicitly. These models are well suited to study the basic behavior of the concrete-reinforcement interface. In *bar-scale* models, the interface is idealized by a cylindrical shape. The local mechanical interaction at the bar-scale must be accounted for indirectly. Therefore, the mechanical interaction is represented either by an increased compliance of the concrete matrix adjacent to the bar or by an increased compliance of the concrete-bar interface. The first approach is simpler, but does not model the wedging effect of the ribs properly. Therefore it is only well suited to capture a pullout failure. The second approach can generally produce both, a pullout and a splitting failure. The third type is the *member scale* model. The reinforcement is usually discretized via a discrete, embedded or smeared model, but other novel approaches to model components have also been developed. Typically, at the member scale model, the reinforcement is treated as a one-dimensional element, and bond laws have been limited to single-stress models and are not swell suited to reproduce the complicated appropriate bond behavior in certain cases.

A bar-scale model is chosen because of the large dimensions of our problems. It is a modification of a model invented by Den Ujil and Bigaj (1996), see Akkermann (2000), and can capture both, a pullout and a splitting failure. It is implemented as user-element in the Finite Element Code ABAQUS and will be described briefly in the following section. Other approaches are given e.g. by Liang et al. (2001, 2002).

Bond forces are transmitted in the concrete by the ribs of the prestressing causing cone-shaped radial cracks in the concrete as shown in Fig. 11. An important parameter is the quotient $\xi = c_{\text{eff}}/D$ of the concrete cover throughout c_{eff} and the diameter D of the rod. If the radial cracks pass through the complete concrete cover throughout, a sudden failure takes place.

The bond model is formulated in terms of the radial stress–radial strain relation. This curve can be split into three domains. The first domain describes the nonlinear material behavior caused by the crack propagation, the second domain is the linear softening domain and the third one is characterized by the residual strength.

Domain 1: $0 \leqslant \epsilon_{r,r_s} \leqslant \epsilon_{r,r_{s,\max}}$

$$\sigma_{r,r_s}(\epsilon_{r,r_s}) = \sigma_{r,r_{s,\max}} \frac{k\eta - \eta^2}{1 + (k-2)\eta} \tag{58}$$

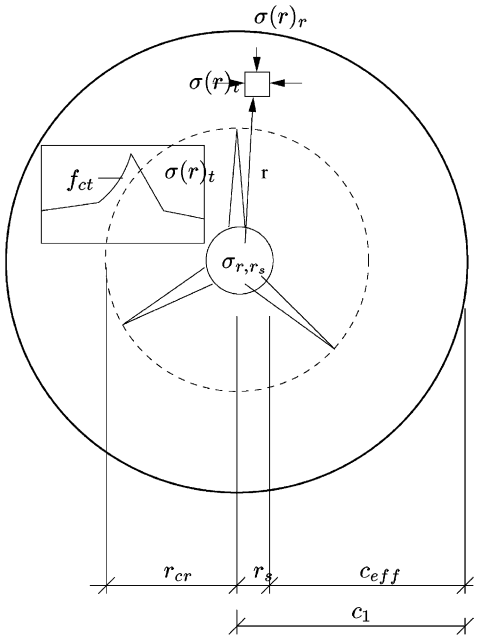

Fig. 11. Bond model with three radial cracks in the concrete.

with

$$k = \frac{E_r \epsilon_{r,r_{s,\max}}}{\sigma_{r,r_{s,\max}}} \quad \eta = \frac{\epsilon_{r,r_s}}{\epsilon_{r,r_{s,\max}}}$$

and the maximum radial stress $\sigma_{r,r_{s,\max}}$ and strain $\epsilon_{r,r_{s,\max}}$, respectively, at failure

$$\sigma_{r,r_{s,\max}} = 2\xi^{0.88} f_{\mathrm{ct}}, \quad \epsilon_{r,r_{s,\max}} = 4.2\xi^{1.08} \frac{f_{\mathrm{ct}}}{E_0} \tag{59}$$

where E_0 is the Young's modulus, f_{ct} is the tensile strength of concrete. The initial stiffness in radial direction is:

$$E_r = E_0 \left(\frac{(c_{\mathrm{eff}} + D/2)^2 + D^2/4}{(c_{\mathrm{eff}} + D/2)^2 - D^2/4} + v \right)^{-1} \tag{60}$$

Domain 2: $\epsilon_{r,r_{s,\max}} < \epsilon_{r,r_s} \leqslant \epsilon_{r,r_{s,\mathrm{res}}}$

$$\sigma_{r,r_s}(\epsilon_{r,r_s}) = \sigma_{r,r_{s,\max}} \left(1 - \frac{1-\psi}{\epsilon_{r,r_{s,\mathrm{res}}} - \epsilon_{r,r_{s,\max}}} (\epsilon_{r,r_s} - \epsilon_{r,r_{s,\max}}) \right), \psi = 0.2 \tag{61}$$

with

$$\epsilon_{r,r_{s,\mathrm{res}}} = (2\xi + c_0/D) \frac{f_{\mathrm{ct}}}{E_0}, c_0 = 0.27m \tag{62}$$

Domain 3: $\epsilon_{r,r_{s,\mathrm{res}}} < \epsilon_{r,r_s}$

$$\sigma_{r,r_s}(\epsilon_{r,r_s}) = \sigma_{r,r_{s,\max}} = \psi \sigma_{r,r_{s,\mathrm{res}}}, \quad \psi = 0.2 \tag{63}$$

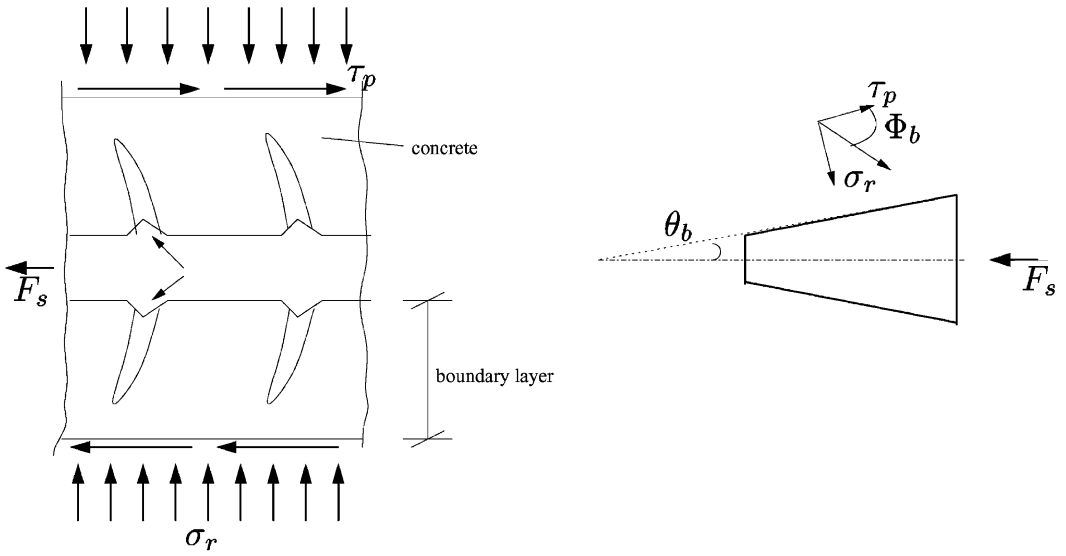

Fig. 12. Bond model.

The bond stresses and the slip has to be defined parallel to the reinforcement. The transmission of the forces from the reinforcement into the concrete can be considered as shown in Fig. 12. The radial strains can be computed from the slip δ_p by

$$\epsilon_{r,r_s}(\delta_p) = \frac{2\delta_p}{D}\tan\vartheta_b \quad \text{with } \vartheta_b = 0.1 f_c \tag{64}$$

where f_c is the compressive strength of the concrete. The bond stress is coupled with the radial stress by a fictive friction

$$\tau_p = \cot\Phi\sigma_{r,r_s} \tag{65}$$

The friction angle depends on the slope of the circumferential cracks and is approximated by $\cot\Phi = 1$. Hence, the bond slip relation is completely determined for a splitting failure.

For a pullout failure, the slip depends on ϑ_b, which decreases with increasing damage of the concrete since the shear resistance of concrete will also decrease. The radial strain can be formulated as function of the slip δ_p and the steel strains ϵ_s

$$\epsilon_{r,r_s} = \frac{f(\delta_p, \epsilon_s)}{r_s} \tag{66}$$

The function $f(\delta_p,\epsilon_s)$ is divided into four parts. A detailed description can be found in Den Ujil and Bigaj (1996). The bond stresses are computed depending on the relevant failure mechanism. Fig. 13a shows the bond slip relations for a splitting failure, Fig. 13b for a pullout failure. For the splitting failure, $\tan\vartheta_b$ is constant and the radial strains depend linear on the slip. For the pullout failure, the radial strains are non-linear dependent on the slip. If the radial stresses are smaller than the maximum slip stresses $\sigma_{r,r_{s,\max}} \leqslant \tau_{p,\max}$ with $\tau_{p,\max} = 5 f_{ct}$, a splitting failure occurs, otherwise a pullout failure.

4.2. Numerical implementation of the bond model

The bond element is implemented in the FE code ABAQUS as user element. It consists of two double nodes (indices i, k and l, m), see Fig. 14. In the initial configuration, the location of the double nodes are

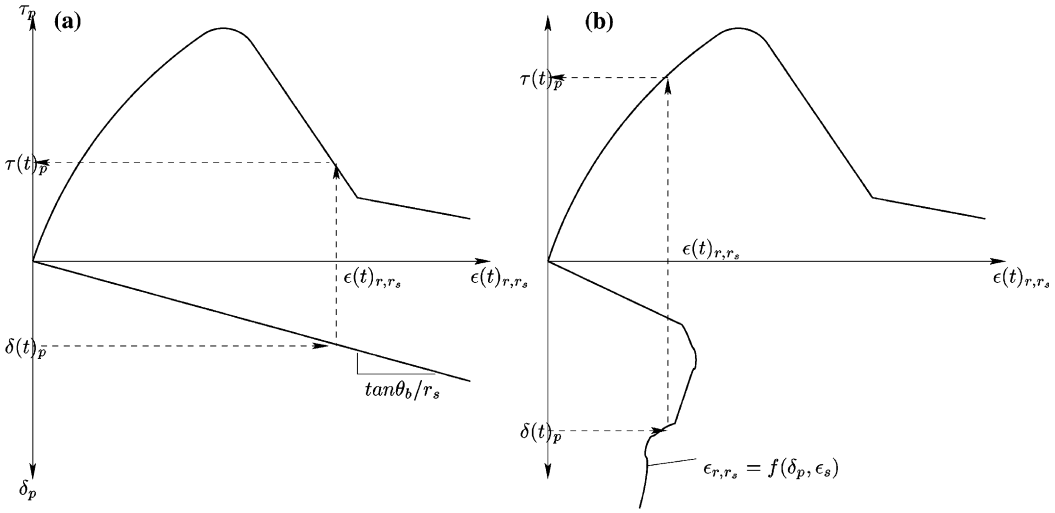

Fig. 13. Bond stress–slip relation for (a) splitting failure and (b) pullout failure.

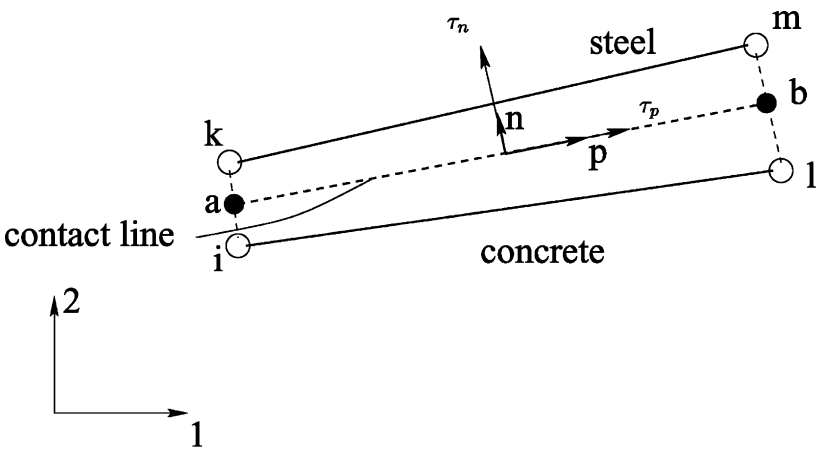

Fig. 14. Bond element.

identical. The nodes i, l correspond to the concrete element and the nodes k, m to the steel element. The contact line is given by the points a and b, see Fig. 14.

Linear shape functions are used which can be formulated in the local coordinate system p, n across the contact line

$$N_1(p) = 0.5(1-p)$$
$$N_2(p) = 0.5(1+p) \tag{67}$$

with $-1 < p < 1$. The global nodal displacement vector $\mathbf{u}$ (global coordinates 1, 2) is then transformed into global relative displacements $\boldsymbol{\delta}_{\mathrm{glob}}(p)$:

$$\boldsymbol{\delta}_{\text{glob}}(p) = \mathbf{B}(p)\mathbf{u}$$

$$\begin{bmatrix}\delta_1(p)\\ \delta_2(p)\end{bmatrix} = \begin{bmatrix}-N_1(p) & 0 & N_1(p) & 0 & -N_2(p) & 0 & N_2(p) & 0\\ 0 & -N_1(p) & 0 & N_1(p) & 0 & -N_2(p) & 0 & N_2(p)\end{bmatrix} \begin{bmatrix}u_{i1}\\ u_{i2}\\ u_{k1}\\ u_{k2}\\ u_{l1}\\ u_{l2}\\ u_{m1}\\ u_{m2}\end{bmatrix} \tag{68}$$

where $\mathbf{B}(p)$ contains the shape functions and *not* the derivatives of the shape functions since the bond stresses depend on the displacements. The relative displacements in the local coordinate system are obtained by a transformation

$$\begin{aligned}&\boldsymbol{\delta}_{\text{lok}}(p) = \bar{\mathbf{T}}\boldsymbol{\delta}_{\text{glob}}(p)\\ &\begin{bmatrix}\delta_p(p)\\ \delta_n(p)\end{bmatrix} = \begin{bmatrix}t_{p1} & t_{p2}\\ t_{n1} & t_{n2}\end{bmatrix}\begin{bmatrix}\delta_1(p)\\ \delta_2(p)\end{bmatrix}\end{aligned} \tag{69}$$

where $\bar{\mathbf{T}}$ is the transformation matrix from the global into the local coordinate system. The unit vectors $\mathbf{t}_p$ and $\mathbf{t}_n$ of the local p, n coordinate system are computed by

$$\begin{aligned}\mathbf{t}_p &= \begin{bmatrix}t_{p1}\\ t_{p2}\end{bmatrix} = \frac{\mathbf{b}-\mathbf{a}}{|\mathbf{b}-\mathbf{a}|}\\ \mathbf{t}_n &= \begin{bmatrix}t_{n1}\\ t_{n2}\end{bmatrix} = \begin{bmatrix}-t_{p2}\\ t_{p1}\end{bmatrix}\end{aligned} \tag{70}$$

where $|\mathbf{b}-\mathbf{a}|$ is the element length l_{el}. The vectors $\mathbf{a}$ and $\mathbf{b}$ in the global coordinate system can be computed by

$$\begin{aligned}\mathbf{a} &= \begin{bmatrix}(i_1-k_1)/2+k_1\\ (i_2-k_2)/2+k_2\end{bmatrix}\\ \mathbf{b} &= \begin{bmatrix}(l_1-m_1)/2+m_1\\ (l_2-m_2)/2+m_2\end{bmatrix}\end{aligned} \tag{71}$$

The element stresses are then obtained by

$$\begin{aligned}\boldsymbol{\tau}(p) &= \mathbf{E}_b\boldsymbol{\delta}_{\text{lok}}(p)\\ \begin{bmatrix}\tau_p(p)\\ \sigma_n(p)\end{bmatrix} &= \begin{bmatrix}E_{bp} & 0\\ 0 & E_{bn}\end{bmatrix}\begin{bmatrix}\delta_p(p)\\ \delta_n(p)\end{bmatrix}\end{aligned} \tag{72}$$

The details about the bond model were given in the previous section. The nodal force vector is obtained by a transformation into the global coordinate system by integration over the element length

$$\mathbf{f}_{\text{el}} = 0.5 l_{\text{el}} \int_{-1}^{1} \mathbf{B}^T(p)(\bar{\mathbf{T}}^T\ \mathbf{A}_b\ \boldsymbol{\tau}(p))\,\mathrm{d}p \tag{73}$$

where $\mathbf{A}_b$ is a contact-area matrix

$$\mathbf{A}_b = \begin{bmatrix}n\ \pi\ d_s & 0\\ 0 & n\ d_s\end{bmatrix} \tag{74}$$

where n is the number of the reinforcement rods and d_s is the diameter of the reinforcement. The stiffness matrix of the element is given by

$$\mathbf{K}_{\mathrm{el}} = 0.5 l_{\mathrm{el}} \int_{-1}^{1} \mathbf{B}^T(p)(\bar{\mathbf{T}}^T\ \mathbf{A}_b\ \mathbf{E}_b(p)\ \bar{\mathbf{T}})\ \mathbf{B}(p)\,\mathrm{d}p \tag{75}$$

Using two point Gauss quadrature, Eqs. (73) and (75) can be written as

$$\mathbf{f}_{\mathrm{el}} = 0.5 l_{\mathrm{el}} \sum_{j=1}^{2} \omega_j \mathbf{B}^T(p_j)(\bar{\mathbf{T}}^T\ \mathbf{A}_b \boldsymbol{\tau}(p_j))\,\mathrm{d}r \tag{76}$$

and

$$\mathbf{K}_{\mathrm{el}} = 0.5 l_{\mathrm{el}} \sum_{j=1}^{2} \omega_j \mathbf{B}^T(p_j)(\bar{\mathbf{T}}^T\ \mathbf{A}_b \mathbf{E}_b(p_j)\ \bar{\mathbf{T}})\ \mathbf{B}(p_j)\,\mathrm{d}r \tag{77}$$

where $p_1 = -1/\sqrt{3}$, $p_2 = -p_1$ and $\omega_1 = \omega_2 = 1$. The steel stresses ϵ_s which are needed for the bond model can be computed corresponding to the elongation of the steel element

$$\epsilon_s = \frac{\overline{\mathbf{km}}^{t} - \overline{\mathbf{km}}^{0}}{\overline{\mathbf{km}}^{0}} \tag{78}$$

5. Results

5.1. Test setup

Three prestressed concrete beams are considered. The first one (beam I) is of rectangular cross section. The test setup and the dimensions of the beam are illustrated in Fig. 16. The beam was prestressed with two tension wires of 7 mm diameter. The upper one was prestressed with a force of 26.25 kN, the lower one with a force of 11.25 kN. The beam failed in bending because of the plastic flow of the lower reinforcement followed by a failure of the concrete compression zone. Fig. 17 shows a cutout of the beam after the experiment. Crack number 2 and 3 are the cracks which caused the failure.

The test setup for the second beam (beam II) is similar to the first one and can be found in Fig. 18. In contrast to the first beam, the second one is of I-cross section. The beam has two tension wires of 12 mm diameter at the lower flange which were prestressed each with a force of 80 kN. The diameter of the upper reinforcement is 10 mm. The beam failed suddenly because of a combined shear/pullout failure as illustrated in Fig. 19a. Crack number 6 caused the failure.

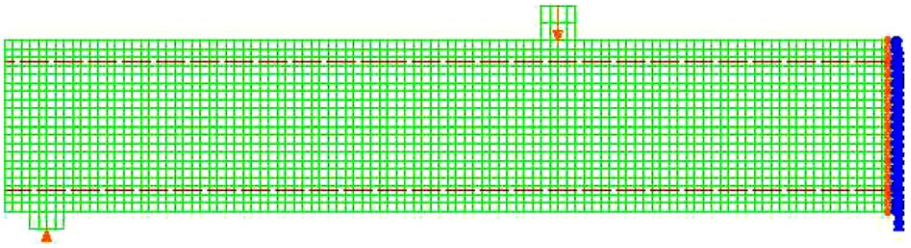

Fig. 15. Finite element discretization with boundary conditions of beam II.

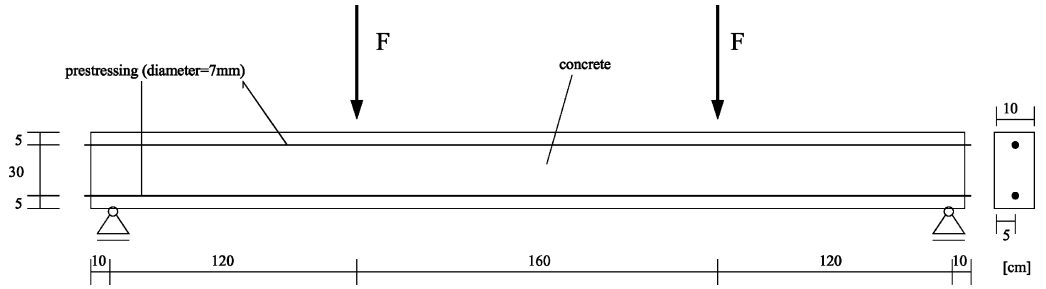

Fig. 16. Test setup of beam I.

Fig. 17. Beam I after the experiment.

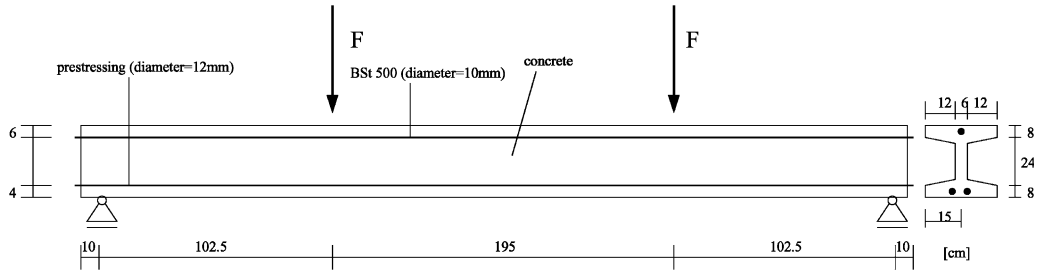

Fig. 18. Test setup of beam II.

(a) (b)

Fig. 19. (a) Beam II after the experiment. (b) Beam III after the experiment.

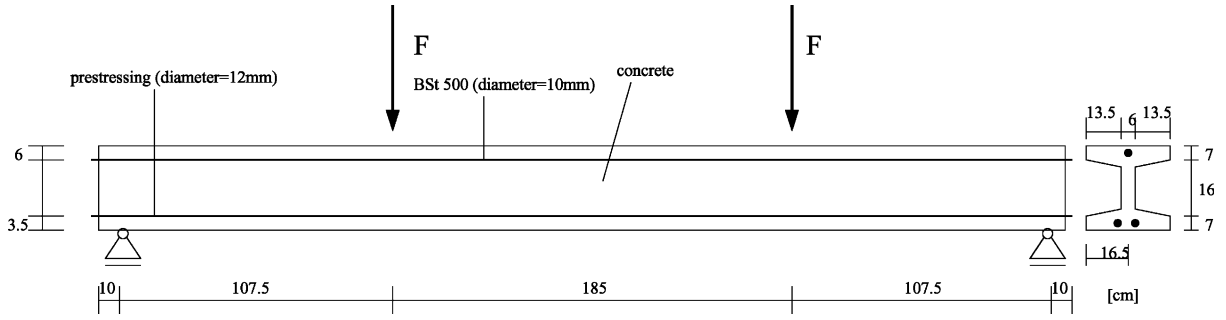

Fig. 20. Test setup of beam III.

The third beam (beam III) has also a I-shaped cross section but the dimensions differ from those of the second beam, see Fig. 20. The beam is prestressed with two tension wires of 12 mm diameter and a force of 68 kN. The same failure mechanism as for beam 2 was observed but the shear crack which caused the failure was farther from the support. More bending cracks appeared and the crack was flatter than in the second experiment. A picture of the beam after the experiment is shown in Fig. 19b. All beams were loaded by a displacement controlled approach. A detailed description about the experiments can be found in Eibl et al. (2001).

5.2. Comparison of the numerical computation with the experiments

All beams are discretized in two-dimensions. Plane stress conditions are assumed. Symmetry conditions were used, meaning only half of the beam is discretized. Two-dimensional plane stress continuum elements (CPS4) with linear shape functions are used for the concrete. Beam elements (B21) with five integration points over the thickness are used for the reinforcement. The stirrup reinforcement for beam I was neglected since it was only needed for transportation purposes. It plays a minor role as similar experiments of prestressed concrete beams showed, see e.g. Eibl et al. (2001). To take into account the interaction between the concrete and the reinforcement, the bond element explained in Section 4 is used.

Fig. 15 shows exemplarily the finite element discretization of beam II with boundary conditions. In the experiment the concrete beam was lying on a steel support. In our computation, the support on the left hand side is connected to the concrete elements and is fixed at the lower side as shown in Fig. 15. Linear elastic material behavior is assumed for the support with a Young's modulus of 2,000,000 MPa . A rubber plate was used in the experiment to load the beam. The load plate is also connected to the concrete beam and linear elastic behavior with a Young's modulus of 10,000 MPa is assumed. A displacement boundary condition is given at the top of the middle of the load plate.

The prestressing is modelled via a temperature loading case of the tension wires. In other words, the tension wire is shortened by cooling down. The strains are computed by $\epsilon = \alpha_t \Delta T$ where α_t is the thermal expansion coefficient which is $1 \times 10^{-5}/C$ for steel and ΔT is the temperature difference, which is negative in our case. The contraction of the tension wire transmits the prestressing forces in the concrete. In the experiments, the tension wires were prestressed first, then the beams were concreted and the prestressing forces were transmitted in the concrete after the desired compressive strength ($=45\,\mathrm{N/mm^2}$) was obtained. All material parameters for the simulation can be found in Tables 2 and 3. For a more detailed description see Eibl et al. (2001).

Table 2
Material parameters for the concrete model

	Beam I	Beam II	Beam III
E_0 [MPa]	26,000	29,000	29,000
v_0	0.2	0.2	0.2
f_{c0} [MPa]	45	45	45
$\epsilon_{c,eff}$	−0.0022	−0.0022	−0.0022
$\epsilon_{ccu,eff}$	−0.0035	−0.0035	−0.0035
f_{t0} [MPa]	2.83	2.83	2.83
G_f [MN/m]	86×10^{-6}	86×10^{-6}	86×10^{-6}

Table 3
Material parameters of the bond model

	f_{ct} [MPa]	f_c [MPa]	c_{eff} [cm]	D [mm]
Beam I	2.83	45	4.5	7.0
Beam II	2.83	45	3.5	12.0
Beam III	2.83	45	3.5	12.0

5.2.1. The bending failure of beam I (VB1)

Fig. 21 compares the computed crack pattern at different load steps (see also Fig. 22) with the experiment. At load step *LS*400, the failure in the experiment is observed. The computation proceeds since no failure model for the reinforcement is used. The calculation reproduces the crack pattern well. At load step *LS*40 a decay in the load mid displacement is observed for the experiment and the simulation, see Fig. 22.

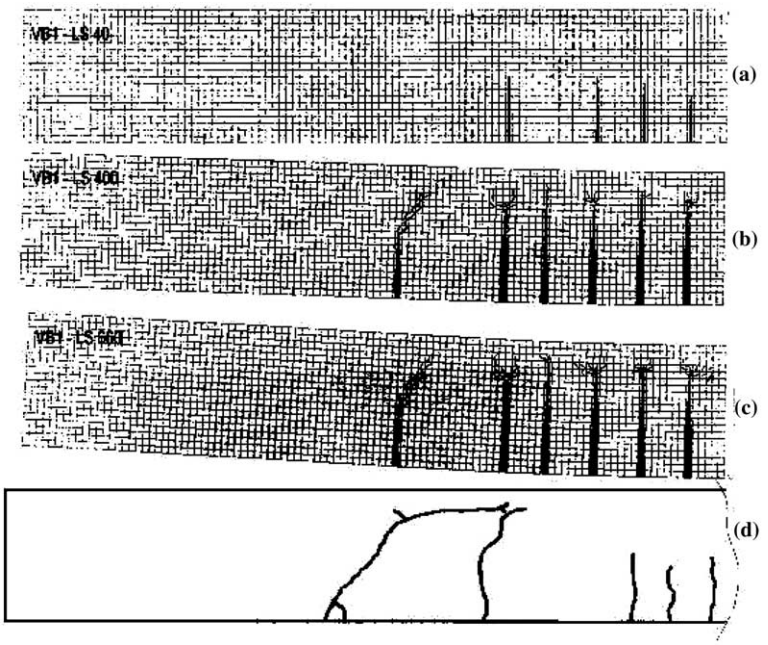

Fig. 21. (a–c) Crack pattern of beam I at different load steps according to Fig. 22, and (d) experimental result.

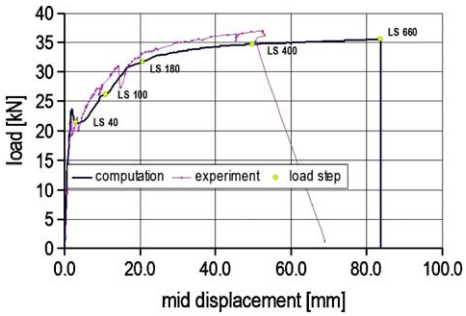

Fig. 22. Experimental and computed load displacement curve of beam I.

This is the point when the first cracks appear. The computation can predict this behavior pretty well. Also the rest of the load mid displacement curve is predicted fair.

5.2.2. The shear/anchorage failure of beam II (VB2) and III (VB3)

In this section the focus will be on beam II. Similar results are obtained for beam III.

Fig. 23 shows the principal stress field in beam II for the loading case prestressing. High tensile stresses can be observed in the middle of the beam over the left support. This matches well with experimental observations where cracking occurs if the beam is prestressed too high. Fig. 24 shows the stresses for the tension wires at different load steps. At the beginning, a uniform distribution can be recognized. After 30 cm from the left support the stresses are completely transmitted in the steel. During loading, the stresses in the reinforcement increase, especially at locations where the concrete cracks (compare with Fig. 25). As in the

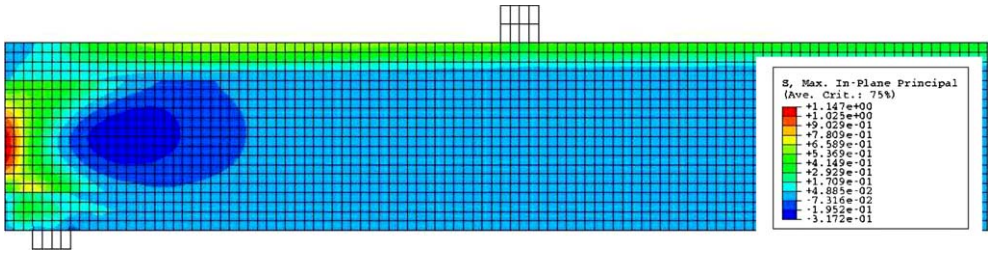

Fig. 23. Principal tensile stress field in the beam for loading case prestressing.

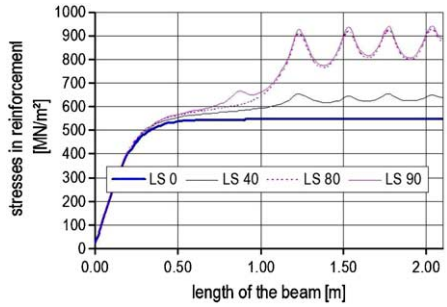

Fig. 24. Stresses in the reinforcement at different load steps for beam II.

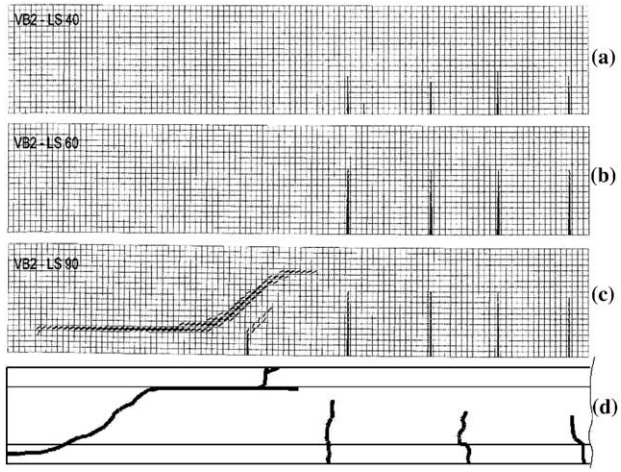

Fig. 25. Experimental and computed crack pattern of beam II at different load steps.

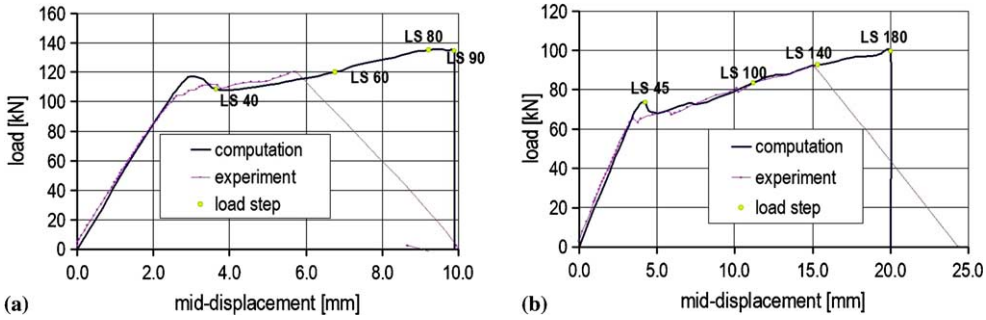

Fig. 26. Experimental and computed load deflection curve for (a) beam II and (b) beam III.

experiment, the tensile strength of the reinforcement is never reached since the concrete beam fails due to a shear failure.

For beam II, Fig. 25 shows the computed cracks to different load steps compared to the experiment. The shear crack in the experiment is closer to the support than in the computation but the computation can predict the principle behavior fair. The computed and experimental load mid-displacement curves for beam II are illustrated in Fig. 26a. The crack initiation is predicted by the simulation quite exact (see also Fig. 25). The rest of the load deflection curve is computed well, too.

The computed load deflection curve compared to the experiment as well as the crack pattern for beam III are shown in Figs. 26b and Fig. 27, respectively. The same observation as for beam II apply here.

6. Summary

Purpose of our study was to model the fracture of reinforced concrete structure taking into account the interaction between concrete and the reinforcement. Therefore, a fictitious/smeared crack approach is proposed. The approach is able to model the anisotropy of concrete in tension. The material behavior in compression is characterized with a non-local scalar damage approach. The constitutive model was

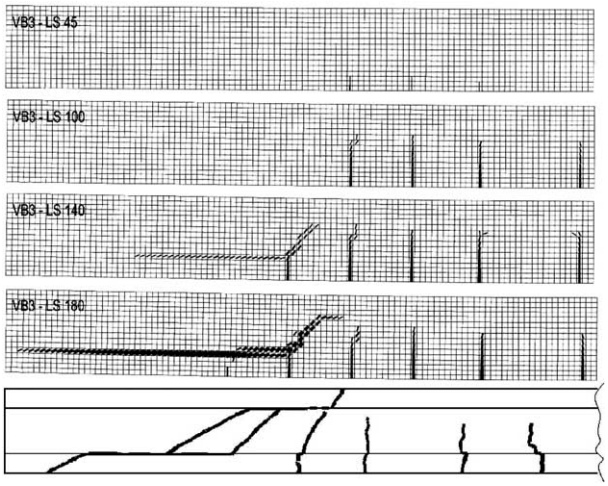

Fig. 27. Experimental and computed crack pattern of beam III at different load steps.

implemented in the FE-code ABAQUS as user subroutine. The reinforcement was described with beam elements using an elastoplastic constitutive model with isotropic hardening. Except of cracking, the interaction between the reinforcement and the adjacent concrete plays a significant role in the fracture process of reinforced concrete structures. A bond model is described which is able to capture both failure mechanisms, a pullout and a splitting failure.

The model is applied to three prestressed concrete beams with different cross sections and different failure mechanisms but also good results were obtained in the application to frame corners, see Akkermann (2000). The first beam failed due to a bending failure, the other beams due to a combined shear and anchorage failure. The numerical results were compared in terms of the crack pattern and load displacement curves and show a fair agreement.

References

Akkermann, J., 2000. Rotationsverhalten von Stahlbeton Rahmenecken; Dissertation, Institut fuer Massivbau und Baustofftechnologie, Universitaet Karlsruhe.

Bazant, Z.P., 1991. Why continuum damage is nonlocal: micromechanics arguments. Journal of Engineering Mechanics 117 (5), 1070–1087.

Bazant, Z.P., 1998. Modelling of compressive strain softening, fracture and size effect in concrete, Computational Modelling of Concrete Structures, de Borst, Bicanic, Mang, Meschke, (Eds.), EURO-C, Balkema, Rotterdam, 249–264.

Bazant, Z.P., Oh, B.H., 1983. Crack band theory for fracture of concrete. Materials and Structures (January–February), 155–177.

Bazant, Z.P., Pihaudier-Gabot, G., 1988. Nonlocal continuum damage, localization instability and convergence. Journal of Applied Mechanics 55, 287–293.

Bazant, Z.P., Prat, P., 1988. Microplane model for brittle plastic materials. I: Theory, II: Verification. Journal of Engineering Mechanics ASCE 114, 1672–1702.

Bazant, Z.P., Ozbolt, J., 1990. Nonlocal microplane model for fracture, damage and size effect in structures. Journal of Engineering Mechanics ASCE 116 (11), 2485–2505.

Bazant, Z.P., Xiang, Y., Prat, P.C., 1996. Microplane model for concrete. I: Stress–strain boundaries and finite strain, II: Data delocalization and verification. Journal of Engineering Mechanics ASCE 122, 245–262.

Bazant, Z.P., Caner, F.C., Carol, I., Adley, M.D., Akers, S.A., 2000. Microplane model M4 for concrete. I: Formulation with work-conjugate deviatoric stress. Journal of Engineering Mechanics ASCE 126, 944–953.

Belytschko, T., Black, T., 1999. Elastic crack growth in finite elements with minimal remeshing. International Journal for Numerical Methods in Engineering 45 (5), 601–620.

Belytschko, T., Lu, Y.Y., 1995. Element-free Galerkin methods for static and dynamic fracture. International Journal of Solids and Structures 32, 2547–2570.

Belytschko, T., Lu, Y.Y., Gu, L., 1994. Element-free Galerkin methods. International Journal for Numerical Methods in Engineering 37, 229–256.

Belytschko, T., Moes, N., Usui, S., 2001. Parimi C.: Arbitrary discontinuities in finite elements. International Journal for Numerical Methods in Engineering 50 (4), 993–1013.

Carol, I., Bazant, Z.P., 1997. Damage and plasticity in microplane theory. International Journal of Solids and Structures 34, 3807–3835.

CEB-FIP MODEL CODE 1990 (MC90), 1993. Design code for concrete structures. Thomas Telford, London.

Cox, J.V., Herrmann, L.R., 1998a. Development of a plasticity bond model for steel reinforcement. Mechanics of Cohesive-Frictional Materials 3, 155–180.

Cox, J.V., Herrmann, L.R., 1998b. Development of a plasticity bond model for steel reinforcement. Mechanics of Cohesive-Frictional Materials 3, 155–180.

Darwin, D., Pecknold, D.A., 1977. Nonlinear biaxial stress–strain law for concrete. Journal of the Engineering Mechanics Division, Proc. of the ASCE 103 (EM2), 229–241.

Den Ujil, J., Bigaj, A.J., 1996. A bondmodel for ribbed bars based on concrete loaded in compression. Heron 41 (3), 201–226.

DeVree, J.H., Brekelmans, W.A.M., vanGils, M.A.J., 1995. Comparison of nonlocal approaches in continuum damage mechanics. Computers and Structures 55 (4), 581–588.

Eibl, J., Neuroth, U., 1988. Untersuchungen zur Druckfestigkeit von bewehrtem Beton bei gleichzeitig wirkendem Querzug, Abschlussbericht, Institut fuer Massivbau und Baustofftechnologie, Universitaet Karlsruhe.

Eibl, J., Stempniewski, L., Rabczuk, T., 2001. Untersuchungen zum Endbereich von im Spannbett vorgefertigten Fertigteiltraegern-Hohlplatten. Abschlussbericht, Institut fuer Massivbau und Baustofftechnologie, Universitaet Karlsruhe.

Etse, G., Willam, K., 1999. Failure analysis of elastoviscoplastic material models. ASCE Journal of Engineering Mechanics 125 (1), 60–69.

Hillerborg, A., Modeer, M., Petersson, P.E., 1976. Analysis of crack formation and crack growth in concrete by means of fracture mechanics and finite elements. Cement and Concrete Research 6, 773–782.

Jansen, D.C., Shah, S.P., 1997. Effect of length on compressive strain softening of concrete. ASCE, Journal of Engineering Mechanics 123 (1).

Jirasek, M., 1993. Modeling of fracture and damage in quasibrittle materials, Ph.D. thesis, Northwestern University, USA.

Jirasek, M., Zimmermann, T., 1998. Rotating crack model with transition to scalar damage. ASCE Journal of Engineering Mechanics 124 (3), 277–284.

Kolleger, J., Mehlhorn, G., 1990. Experimentelle Untersuchungen zur Bestimmung der Druckfestigkeit des gerissenen Stahlbetons bei einer Querzugbeanspruchung, DAfStb Heft 413, Berlin, Germany.

Kupfer, H., 1973. Das Verhalten des Betons unter mehrachsiger Kurzzeitbelastung unter besonderer Beruecksichtigung der zweiachsigen Beanspruchung, DAfStb Heft 229, Berlin, Germany.

Lemaitre, L., 1971. Evaluation of dissipation and damage in metal submitted to dynamic loading, In: Proceedings ICM 1.

Liang, Q.Q., Xie, Y.M., Steven, G.P., 2001. Generating optimal srut-and-tie models in prestressed concrete beams by performance-based optimazation. ACI Structural Journal 98 (2), 226–232.

Liang, Q.Q., Uy, B., Steven, G.P., 2002. Performance-based optimization for stut-tie modeling of structural concrete. Journal of Structural Engineering ASCE 128 (6), 815–823.

Markeset, G., Hillerborg, A., 1995. Softening of concrete in compression-localization and size effects. Cement and Concrete Research 25 (4), 702–708.

Meyer, J., Koenig, G., 1998. Verformungsfaehigkeit der Betonbiegedruckzone-Spannungs-Dehnungs-Linien fuer die nichtlineare Berechnung, Beton- und Stahlbeton 93, Heft 7, pp. 189–194, Heft 8, pp. 224–228.

Ozbolt, J., 1995. Massstabseffekt und Duktilitaet von Beton- und Stahlbetonkonstruktionen, Habilitationsschrift. Institut fuer Werkstoffe im Bauwesen, Universitaet Stuttgart.

Ramm, E., 1981. Strategies for tracing nonlinear response near limit points. In: Wunderlich, E. (Ed.), Nonlinear Finite Element Analysis in Structural Mechanics. Springer Verlag, Berlin, pp. 63–89.

Rots, J.G., 1988. Computational modeling of concrete fracture. Ph.D. thesis, Delft University of Technology.

Rots, J.G., 1992. Removal of finite elements in strain-softening analysis of tensile fracture. In: Bazant, Z.P. (Ed.), Proceeding of the First International Conference on Fracture Mechanics of concrete Structures FraMCoS1. Elsevier Applied Science, London, New York, pp. 330–338.

Roelfstra, P.E., Wittmann, F.H., 1986. Numerical method to link strain softening with failure of concrete. In: Wittmann, F.H. (Ed.), Fracture Toughness and Fracture Energy of Concrete. Elsevier, pp. 164–175.

Samaniego, E., Oliver, X., Huespe, A., 2003. Contributions to the continuum modelling of strong discontinuities on two-dimensional solids. Monograph CIMNE No. 72, International Center for Numerical Methods in Engineering, Barcelona, Spain.

Schweitzerhof, K., 1989. Quasi-Newton Verfahren und Kurvenverfolgungsalgorithmen fuer die Loesung nichtlinearer Gleichungssysteme in der Strukturmechanik. Institut fuer Baustatik, Unversitaet Karlsruhe.

Sluys, L.J., 1992. Wave propagation, localisation and dispersion in softening solids. PhD thesis, TH Delft.

Walraven, J.C., 1980. Aggregate Interlock: A theoretical and epxerimental analysis. Ph.D. thesis, TH Delft.

van Mier, J.G.M., 1984. Strain softening of concrete under multiaxial loading conditions. Ph.D. thesis, TU Eindhoven.

van Mier, J.G.M., Shah, S.P. et al., 1997. Strain-softening of concrete in uniaxial compression. Materials and Structures 30, 195–209.

Vonk, R.A., 1993. A micromechanical investigation of softening of concrete loaded in compression. Heron 38 (3).

Wells, G.N., Sluys, L.J., 2001. A new method for modelling cohesive cracks using finite elements. International Journal for Numerical Methods in Engineering 50, 2667–2682.

Willam, K., Pramono, E., Sture, S., 1987. Fundamental issues of smeared crack models. SEM/RILEM International Conference on Fracture of Concrete and Rock, Houston, Texas, June.

Xu, X.P., Needleman, A., 1996. Numerical simulations of dynamic crack growth along an interface. International Journal of Fracture 74 (4), 289–324.